Results in Engineering 19 (2023) 101305

Contents lists available at ScienceDirect

Results in Engineering

journal homepage: www.sciencedirect.com/journal/results-in-engineering

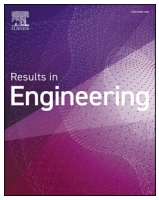

Tribocorrosion behaviour of NiTiNOL60 alloy in an alkaline environment

Anthony Okoani [a,c,**], Ashveen Nand [b], Maziar Ramezani [a,*]

[a] Department of Mechanical Engineering, Auckland University of Technology, Auckland, New Zealand
[b] Faculty of Engineering, University of Auckland, Auckland, New Zealand
[c] Department of Mechanical Engineering, University of Nigeria, Nsukka, Nigeria

ARTICLE INFO

Keywords:
NaOH electrolyte
NiTiNOL60 alloy
Sliding wear
Tribocorrosion

ABSTRACT

NiTi-based alloys subjected to aggressive tribocorrosion working conditions can deteriorate by the combined action of mechanical and chemical wear. The synergistic interaction under sliding contact and corrosive environment formed the basis of the current study. This study employed a linear reciprocating tribometer coupled with an electrochemical cell of a three-electrode configuration to investigate the behaviour of NiTiNOL60 alloy sliding against an alumina ball (Al_2O_3) in a NaOH environment. The resulting wear track surfaces were examined using a scanning electron microscope, optical microscope, energy dispersive spectroscopy (EDS), and stylus profilometry. While the synergistic interactions reveal that abrasive and oxidative wear mechanisms exist concurrently, an increase in applied load reduces the corrosion potential, thereby leading to a higher wear volume and increased corrosion rate. The experimental results showed that a higher corrosion rate and wear volume occurred at a higher load. The wear track analysis illuminated the various wear mechanisms at play, including abrasion, debris adhesion, pitting, delamination, ploughing, and cracking. These mechanisms were influenced by both mechanical and chemical wear, the latter notably due to corrosive attacks. EDS elemental analysis showed an increase in oxygen content at higher loads, which suggests increased corrosion due to the delamination of the oxide layer during the reciprocating sliding.

1. Introduction

Tribocorrosion, a phenomenon where the combined effects of mechanical wear and chemical corrosion lead to material degradation [1,2], has become a research hotspot in recent years due to its significant impact on the performance and longevity of metallic materials in various demanding environments. Understanding the tribocorrosion behaviour of different materials is crucial to enhancing the durability and efficiency of systems in which these materials are employed [3]. Traditionally, 316 L stainless steel has been used in load-bearing applications in corrosive environments [4] such as liquid-handling systems and hydraulic machinery. This is attributed to its impressive mechanical properties, excellent formability, relatively low cost, and good corrosion resistance [5–7]. However, the low resistance of the steel-grade materials to localised corrosion, tribocorrosion wear, and cavitation erosion as a result of low hardness (around 200 HV) limits their use in aggressive environments [6]. highlighted that more than 80% of machine failures are caused by abrasion on the surface of the component. These support the concern around the increasing rate of product contamination and surface deterioration of equipment in the process industries (food and beverage, pharmaceutical, etc.) arising from mechanical loading and harsh corrosive conditions [8,9]. Metals in various flow systems, such as chemical reactors are prone to tribocorrosion. In such systems, the corrosion attack on the metal surface in the corrosive environment is accelerated by the fluid flow, while the wear occurs due to mechanical loading and/or sliding contact [2,9]. Thus, it is imperative that the synergistic interactions of sliding wear and electrochemical reactions in a corrosive environment be investigated [10,11]. The tribocorrosion study ideally involves the integration of a tribometer and a potentiostat in a controlled system. The tribometer provides controlled mechanical loading and relative motion and measures the friction force, while the potentiostat determines open-circuit potential (OCP) and electrochemical measurements [12].

NiTiNOL60, also known as 60NiTi, is a binary nickel-titanium alloy containing 60 wt% Ni and 40 wt% Ti which has been shown to achieve the highest hardness amongst the binary compounds after heat treatment at 1050 °C [13]. It was first discovered by William J. Buehler and his colleagues in the late 1950s at the Naval Ordnance Laboratory,

* Corresponding author.
** Corresponding author. Department of Mechanical Engineering, Auckland University of Technology, Auckland, New Zealand.
E-mail addresses: anthony.okoani@aut.ac.nz (A. Okoani), maziar.ramezani@aut.ac.nz (M. Ramezani).

https://doi.org/10.1016/j.rineng.2023.101305
Received 25 May 2023; Received in revised form 5 July 2023; Accepted 18 July 2023
Available online 20 July 2023

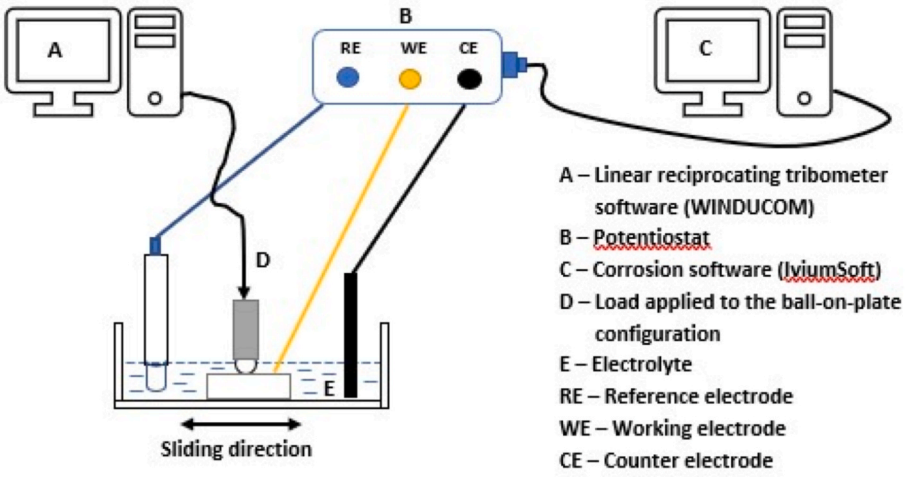

Fig. 1. Schematic of a reciprocating tribocorrosion ball-on-plate setup.

Maryland, USA; this gave rise to the name NiTiNOL (Nickel–Titanium Naval Ordnance Lab) commonly used for 60NiTi alloy [14–16]. The non-equiatomic phase of the Ni-rich (NiTiNOL60) alloy differs from the equiatomic shape memory alloy. NiTiNOL60 is an ordered intermetallic material compound consisting of a B2, cubic crystal structure matrix containing one or more secondary phases including the metastable NiTi and Ni_3Ti_2 phases, and the equilibrium Ni_3Ti phase also referred to as globular Ni_3Ti precipitates [17,18]. In general, NiTiNOL60 alloy is a versatile material owing to its unique properties and wide range of applications from aerospace, automotive, turbine blades [19] and actuators [20,21] in various engineering fields to medical devices and biomechanics [22–26]. In addition, Nickel alloys have an excellent track record for providing corrosion resistance, and high strength at high temperatures in various applications, thereby making the material an enviro-metal [23]. However, the cost of NiTi-based alloys limits their use in most desirable applications.

The material properties of NiTi alloys have been investigated by several researchers. DellaCorte [27]. and [48] investigated the superelastic behaviour of NiTiNOL60 material for space bearing. Du et al. [6] reported that NiTiNOL60 coating on 316 L stainless steel substrate remarkably improves corrosion resistance. Zhang et al. [28] showed that magnetron sputtering coating of NiTiNOL60 alloy improved the hardness and corrosion resistance when compared with 316 stainless steel substrates. [49,50] investigated the sliding wear behaviour of NiTi alloys under dry and lubricated contacts and determined their wear mechanisms under different working conditions.

Kosec et al. [29] studied the effects of different microstructures on tribocorrosion behaviour of NiTi alloys in simulated saliva. Yan et al. [30] studied the microstructure and tribocorrosion performance of NiTiNOL60 alloy in artificial seawater. They identified B2 TiNi and stable $TiNi_3$ phases in the as-cast NiTiNOL60. They reported that solution treatment could lead to the precipitation for metastable Ti_3Ni_4 phase in the matrix without dissolving the $TiNi_3$ phase completely. Meanwhile, Chen et al. [31] demonstrated that B2–NiTi phase transformed into a martensite B19′-NiTi phase during tribocorrosion process. In addition, they highlighted that some tiny pits at the interface of the phases could attribute to the wear contact stresses accelerating corrosion effect. Xu et al. [32] investigated the synergistic interactions between wear and corrosion of Ti–16Mo orthopaedic alloy. They reported that corrosion rate increases under sliding contact. Thus, they concluded that corrosion and wear accelerate each other significantly, with a reported corrosion rate and wear rate increase of about 100 times and 40%, respectively, under tribocorrosion in Ringer's simulated body fluid.

While literature information reveals that most tribocorrosion studies conducted so far were focused on environments such as acidic, sea water and simulated body fluids, there is a research gap on understanding the tribocorrosion performance of NiTiNOL60 alloy in alkaline environment. Therefore, in this paper, we investigated the tribobocorrosion behaviour of NiTiNOL60 alloy in NaOH (caustic soda) environment which is peculiar to a variety of manufacturing processes as a cleaning agent due to its effectiveness in dissolving greases, fats, and protein-based deposits. Understanding how an alkaline environment impacts the tribocorrosion of NiTiNOL60 alloy can provide valuable insights into enhancing the alloy's lifespan and effectiveness in various applications.

2. Materials and methods

The NiTiNOL60 samples were received from the National Aeronautics and Space Administration (NASA), Glenn Research Center in Cleveland, Ohio. The samples were manufactured through Hot Isostatic Pressing (HIP) method. Detailed information about the fabrication process of the NiTiNOL60 components can be found in Stanford (2015). The samples were grinded with sandpapers of #180, 500, 1200, and 2400 grits with corresponding grain sizes of 104, 35, 15, and 8 μm respectively. Afterward, the samples were mechanically polished using diamond paste (6 μm and 1 μm) on a polishing surface of 6 μm and 1 μm respectively, for a mirror surface finish. The polished samples were ultrasonically cleaned in 98% (absolute) ethanol for 3 min and then dried with compressed air.

Subsequently, the micro-structural examinations (morphology and the elemental composition) were carried out on the prepared samples using a scanning electron microscope (SEM – Hitachi SU-70 model) at varying magnifications and an energy dispersion spectroscopy (EDS – Hitachi SU-70 model) was conducted to ascertain the elemental distribution in certain regions/phases. Further, the microhardness and surface roughness were measured using a Leco LM-800AT Rockwell hardness tester and a Talysurf 50 Taylor Hobson stylus profilometer.

The setup for tribocorrosion investigation involved the integration of a tribometer and an electrochemical system. The choice of the electrochemical technique for a tribocorrosion test depends on the sliding contact conditions (rotary or linear reciprocating), the two surfaces set in motion, and the shape of the specimen. In this research, we adopted the standard practice for electrochemical measurements in linear reciprocating contact [33,34] to measure the current between the anode and cathode terminals of the sample. The tribocorrosion configuration is based on ASTM standard test methods for linear reciprocating ball-on-flat sliding and the synergy between wear and corrosion [35,36]. As shown in Figure (1), the setup is a configuration consisting of a linear reciprocating ball-on-plate tribometer (DUCOM TR-282) coupled with a

Table 1
Sliding wear test conditions.

Load (N)	Frequency (Hz)	Stroke length (mm)	Temperature (°C)
2, 5, 8	4	10	Room temperature (22 °C)

Table 2
Electrochemical testing parameters.

Parameter	Value
Potential (V)	−5.0 to +7.5
Scan rate (mV/s)	2.0
Potential step (mV)	100
Sample period (s)	700
Conditioning/stabilisation time (s)	1200

three-electrode electrochemical cell (IviumStat) in a 0.05 M NaOH environment/electrolyte at room temperature.

Graphite rod and calomel electrodes were used as the counter electrode (CE) and reference electrode (RE), respectively, while the NiTiNOL60 plates (with dimensions of 20 mm × 10 mm × 10 mm) served as the working electrode (WE). As reported by Ref. [37]; one of the contacting bodies is kept as an insulator and the conductive body is used as the testing sample for tribocorrosive analyses. As a result, only the top part of the sample was exposed, while the other parts of the sample were insulated/coated. The sliding wear tests were conducted using a 10 mm diameter alumina (Al_2O_3) ball as the counter-body with a fresh surface revealed for each test. During the test, the sliding frequency was constant at 4 Hz under different applied normal loads as shown in Table 1 and a stroke length of 10 mm was applied, with a total sliding distance of 500 m.

Before the potentiodynamic polarisation measurements, the prepared sample with an exposed surface area 2 cm^2 was fully submerged in the electrolyte for open circuit potential (OCP) measurements until a stabilisation state was attained. The parameters used for the electrochemical measurements are shown in Table 2 and the measurements were carried out using IVIUM Vertex potentiostat. Each tribocorrosion test was repeated at least three times and the average values of the results are reported.

Surface characterisations were carried out on the wear tracks after the tribocorrosion experiments. A scanning electron microscope (SEM) coupled with energy dispersive spectroscopy (EDS) (Hitachi SU-70 model) was used to observe the surface morphology of the wear track as well as the elements distribution and chemical state of the samples. The wear tracks were examined using optical microscope and stylus profiler to ascertain the material loss and wear volume. The wear volume recorded from tribocorrosion is due to a combined actions of sliding wear and the electrochemical interactions. The synergistic wears can be quantified using the following equation presented by Ref. [30]:

$$T = W_o + C_o + \Delta C_w + \Delta W_c \quad (1)$$

where W_o is the mechanical wear rate, C_o is the electrochemical corrosion rate, ΔC_w is the corrosion due to wear, ΔWc represents wear due to corrosion and T represents the total material loss rate.

According to Archard law, the wear volume is proportional to the normal force and the sliding distance, and inversely proportional to the hardness of the specimen, as presented in the following equation:

$$V \propto \frac{w.d}{H} \quad (2)$$

where V is the wear volume loss, w represents the normal load, d is the total sliding distance, and H is the hardness of the wearing body. To measure the wear volume, five different areas of each wear track were examined using the stylus profilometer, which allowed us to generate a raw profile chart of the sample's worn surface. This examination facilitated the measurement of the depth and width of the wear scars. We used Image J, a software tool for image analysis, to calculate the average surface area of the wear scars. By multiplying the average cross-sectional area by the length of the wear track (10 mm), we determined the volume of wear loss. And the specific wear rate was then calculated using the following equation:

$$\dot{W}\left(mm^3 / Nm\right) = \frac{V}{w.d} \quad (3)$$

Equation (4) shows the Butler-Volmer equation i.e., a combined Tafel equations for the cathodic and anodic reactions in an electrochemical system.

$$I = I_{corr}\left(e^{\frac{2.303(E-E_{corr})}{\beta_a}} - e^{\frac{-2.303(E-E_{corr})}{\beta_c}}\right) \quad (4)$$

where I is current, I_{corr} is the corrosion current, E is applied potential,

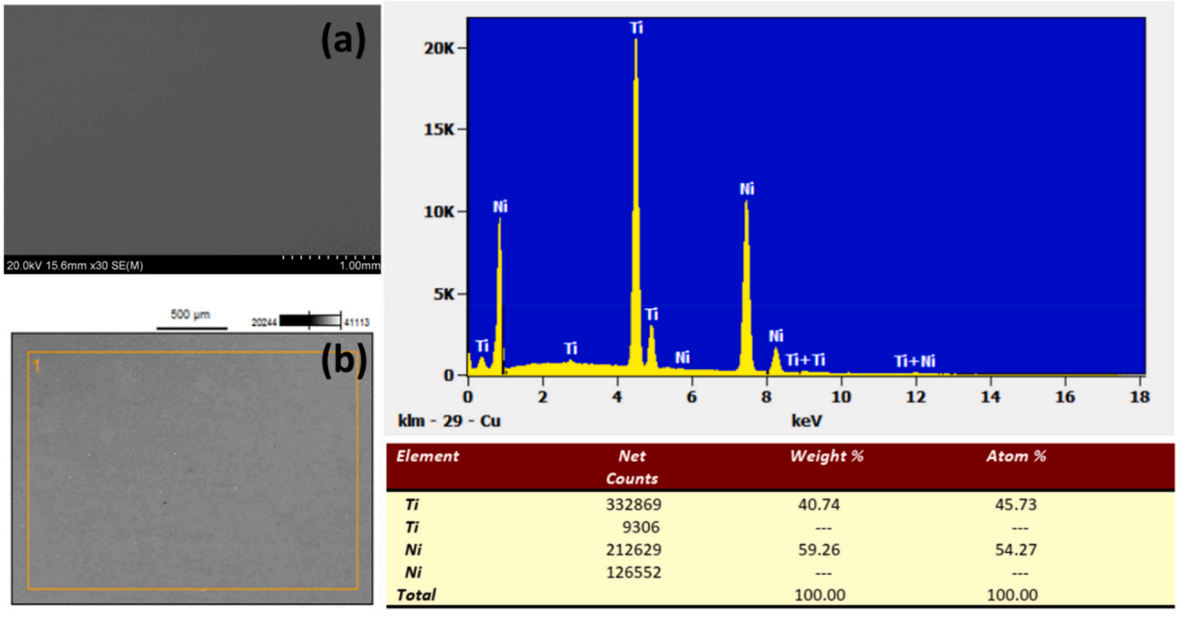

Element	Net Counts	Weight %	Atom %
Ti	332869	40.74	45.73
Ti	9306	---	---
Ni	212629	59.26	54.27
Ni	126552	---	---
Total		100.00	100.00

Fig. 2. SEM and EDS results of a plain NiTiNOL60 sample.

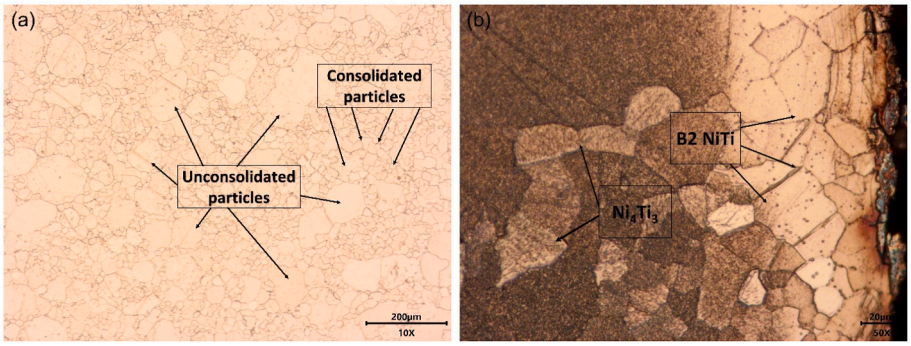

Fig. 3. Microstructure of NiTiNOL60 samples showing unconsolidated and uniformly consolidated particles.

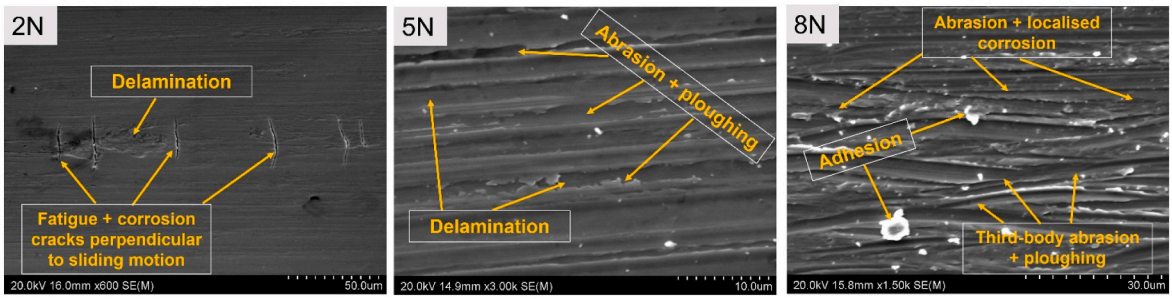

Fig. 4. SEM images showing the wear track microstructure of NiTiNOL60 alloy sample under different mechanical loads.

E_{corr} is the corrosion potential, and β_a and β_c are the Tafel constants or Tafel parameters derived from E − log I plots as the anodic and cathodic slopes in the Tafel regions, respectively. This equation has been used to obtain the polarisation curves and corrosion rates.

3. Results and discussions

3.1. Sample characterisation

The SEM image and EDS analysis of the NiTiNOL60 sample are presented in Fig. 2. A full-scale scan with a penetrating voltage of 20 KV was used to examine the sample surface. The use of a high penetrating voltage ensures the generation of X-rays from deeper within the sample, thereby providing a comprehensive analysis of the surface as well as the subsurface regions of the sample. As seen from the EDS micrograph and the accompanying data table, it is confirmed that the sample under investigation is a nickel rich Ni–Ti alloy having the wt.% compositions of 60 wt% Ni and 40 wt% Ti.

The microstructure of the samples was also examined using an optical microscope (AMScope – Olympus BX51 M model). The microstructure of the cross-sectional sample obtained through wire-cutting is depicted in Fig. 3. Fig. 3(a) represents a plain view of the sample's microstructure whereas further examination under the wear track region is presented in Fig. 3(b). The micrographs shown in Fig. 3 confirm that NiTiNOL60 alloy is an ordered intermetallic material compound consisting of cubic crystal structure matrix, which is consistent with observations by earlier researchers [17,38]. The microstructural grains show consolidated and unconsolidated regions. This could be attributed to the non-equiatomic composition of the NiTiNOL60 alloy thus, the tendencies of Ni-rich or Ti-rich zones. This shows a dominance of B2 NiTi matrix and Ni_4Ti_3 phases, which [51,52] presented the phases as cubic and rhombohedral crystal structures. The results of the Rockwell hardness tests showed an average hardness of 62.5 HRC for the samples. After the tribocorrosion tests, the hardness on the wear track slightly increased to 63.75 HRC, which could be due to the oxide layer formation as will be discussed in the following section.

Further examination of the wear track after the tribocorrosion tests under different loads and electrochemical conditions reveal abrasion, debris adhesion, pits, delamination, plough and cracks, as seen in Fig. 4. Both mechanical and chemical wears which occurred as a result of sliding contact and corrosion attacks are clearly shown from the images. The localised corrosion (pits, cracks and crevices) observed on the surface occurred as a result of the oxidised layer on the exposed surface, supported by the electrochemical reactions during the open circuit potential and the potentiodynamic polarisation [39]. Microcracks (perpendicular to the sliding direction) and delamination were also observed along the wear tracks. According to Ref. [40]; corrosion pits can also promote the nucleation of fatigue crack by providing stress concentration.

EDS elemental analysis of selected areas revealed the elemental compositions at various point scans as shown in Fig. 5. From the table, the EDS analysis for some selected areas exhibits an increase in oxygen content at higher loads, while no oxygen element was detected for 2 N load. According to Ref. [30]; this indicated that the exfoliation or delamination of the oxide layer during the reciprocating sliding exposes the surface of the alloy to the corrosive medium and thus, accelerates the corrosion of the material.

At 2 N and 5 N, the formation of Ti–Ti phase indicates the likely occurrence of TiO_2 following the oxide layer whereas Ti–Ni occurred at 8 N. From the tables in Fig. 5, it is clear that more oxide layer was formed at applied load of 8 N, and this could be attributed to the larger surface area created during the sliding action. This is due to the larger wear track width and wear volumes for sliding wear tests conducted at higher applied loads. Also, the counter material (Al_2O_3) deposits on the wear track increases at higher load. Fig. 6 shows the SEM images for the different Al_2O_3 balls used for sliding tests.

Further EDS analyses were conducted to determine the elemental composition of the debris adhered on the alumina ball. Fig. 7 presents the spectral imaging and elemental composition in wt.%. Of the alumina ball after a tribocorrosion test conducted under 4 Hz sliding frequency and 8 N load. The detected carbon at different points examined could be as a result of some carbonaceous materials within the EDS chamber.

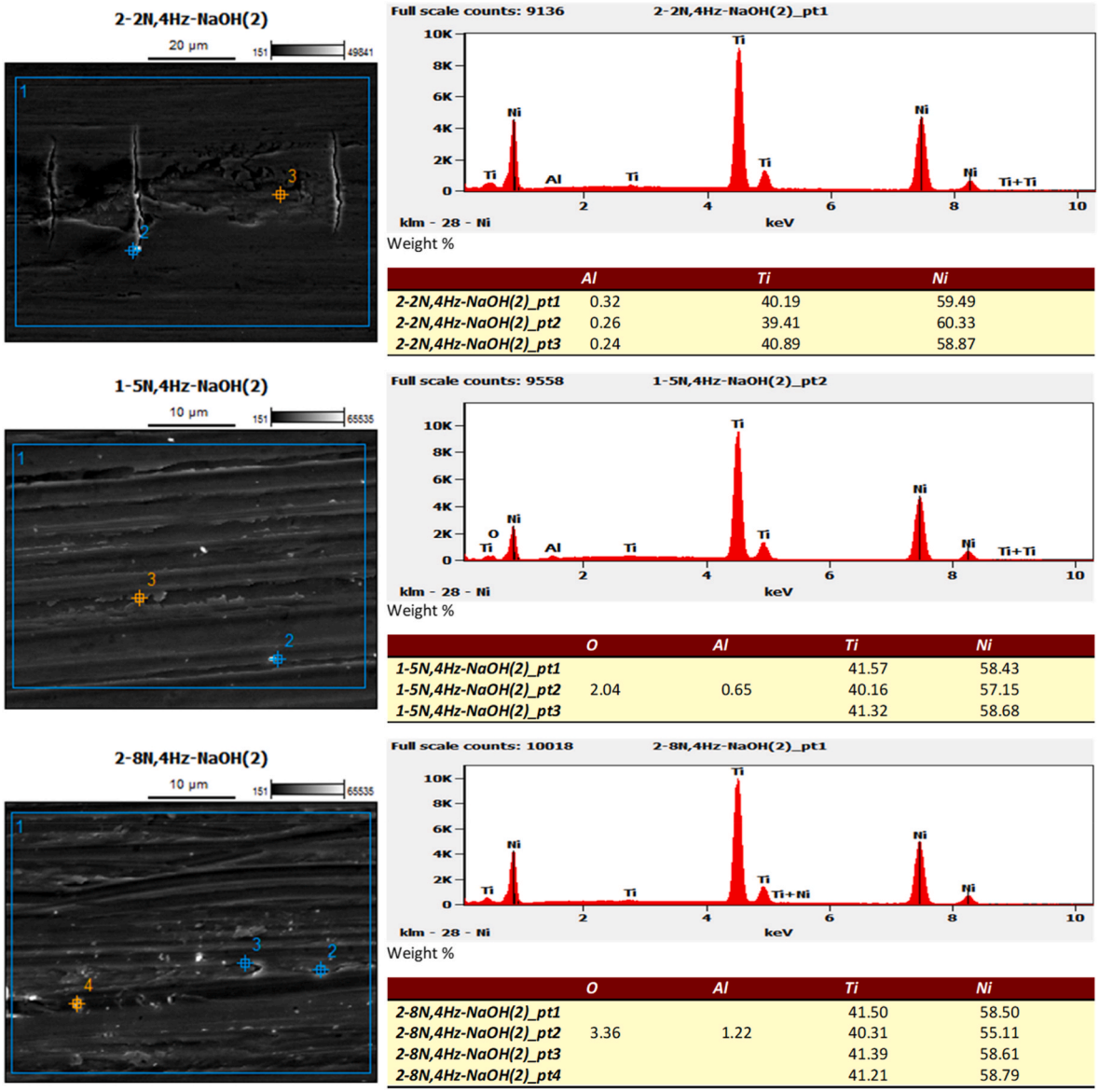

	Al	Ti	Ni
2-2N,4Hz-NaOH(2)_pt1	0.32	40.19	59.49
2-2N,4Hz-NaOH(2)_pt2	0.26	39.41	60.33
2-2N,4Hz-NaOH(2)_pt3	0.24	40.89	58.87

	O	Al	Ti	Ni
1-5N,4Hz-NaOH(2)_pt1			41.57	58.43
1-5N,4Hz-NaOH(2)_pt2	2.04	0.65	40.16	57.15
1-5N,4Hz-NaOH(2)_pt3			41.32	58.68

	O	Al	Ti	Ni
2-8N,4Hz-NaOH(2)_pt1			41.50	58.50
2-8N,4Hz-NaOH(2)_pt2	3.36	1.22	40.31	55.11
2-8N,4Hz-NaOH(2)_pt3			41.39	58.61
2-8N,4Hz-NaOH(2)_pt4			41.21	58.79

Fig. 5. EDS analysis for the wear track of NiTiNOL60 at different applied loads.

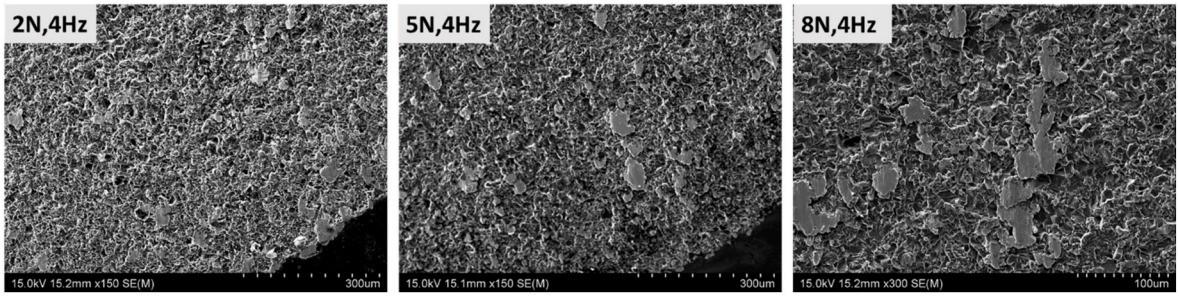

Fig. 6. SEM images of Al_2O_3 balls after reciprocating sliding actions.

Point 1 gives the overall scan of the surface examined and the identified elements are listed in the accompanying table. While the high percentage composition of Ni and Ti at point 2 confirms the adhesion of NiTiNOL60 debris, points 3 and 4 show the composition of the counter material (Al_2O_3) without adhesion of the NiTiNOL60 debris.

Further EDS analysis on the wear tracks of the sample tested at the higher load of 8 N was carried out and the results are presented in Fig. 8. It is noted that more oxide layers occur during repassivation whereas in lower loads where the contact pressure is insignificant, the formation of passive film on the anode surface hinders the reaction between the anode surface and the solution. As the passive film gradually dissolves, the reaction tends to balance, and the potential tends to be stable [6].

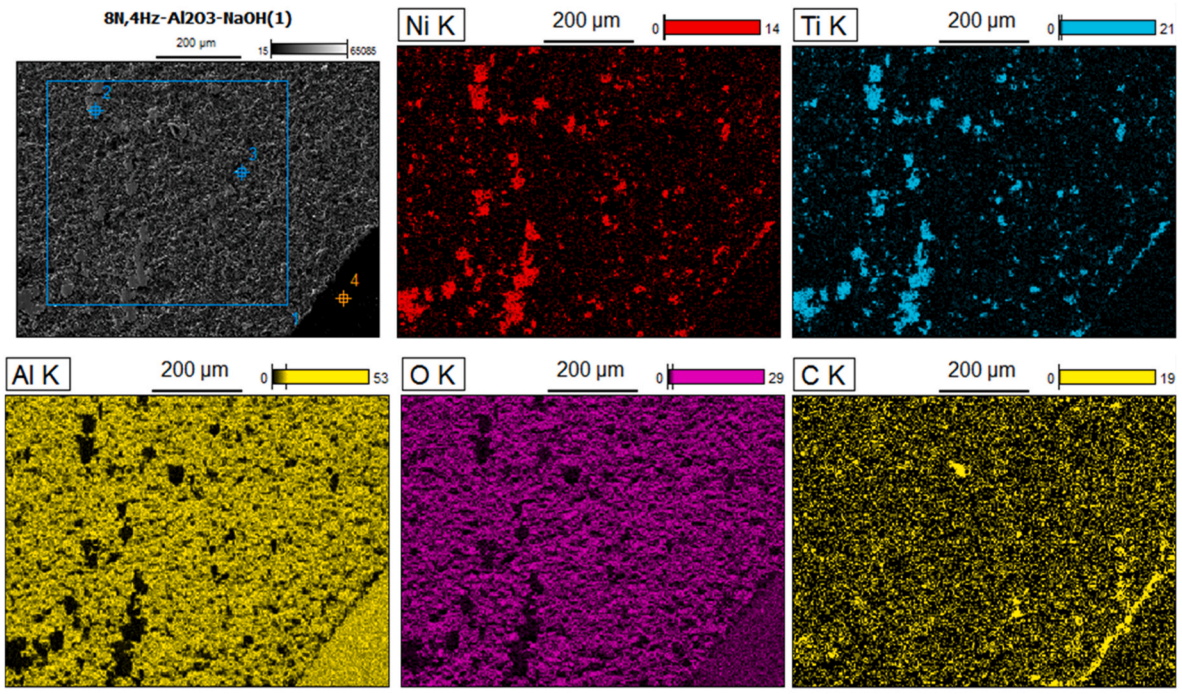

	C	O	Al	Ti	Ni
8N,4Hz-Al2O3-NaOH(1)_pt1	6.84	41.77	40.39	4.17	6.82
8N,4Hz-Al2O3-NaOH(1)_pt2	2.11		1.39	38.98	57.52
8N,4Hz-Al2O3-NaOH(1)_pt3	3.84	51.22	44.94		
8N,4Hz-Al2O3-NaOH(1)_pt4	3.69	38.73	57.58		

Fig. 7. Spectral imaging and EDS composition of Al_2O_3 ball after tribocorrosion test conducted at 8 N load and 4 Hz frequency.

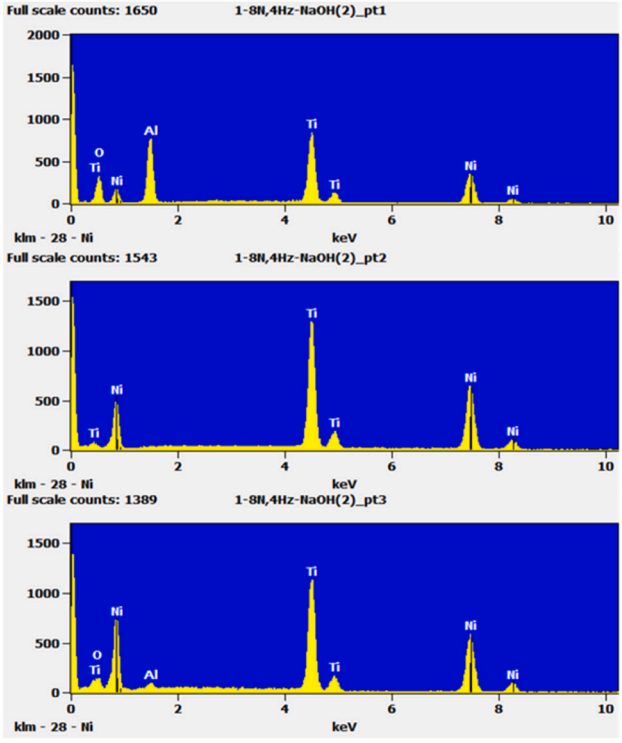

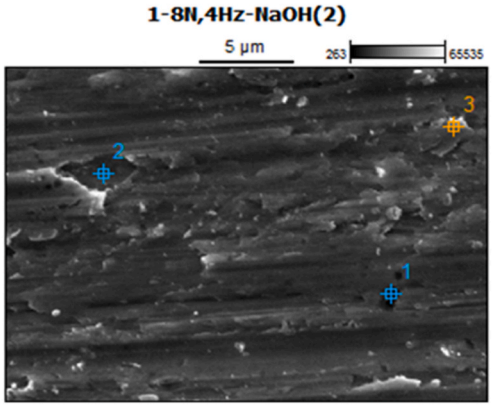

Weight %

	O	Al	Ti	Ni
1-8N,4Hz-NaOH(2)_pt1	30.16	15.90	24.34	29.61
1-8N,4Hz-NaOH(2)_pt2			41.77	58.23
1-8N,4Hz-NaOH(2)_pt3	9.93	1.36	36.60	52.10

Fig. 8. EDS examination of the wear track of the NiTiNOL60 sample tested at 8 N load and 4 Hz sliding frequency.

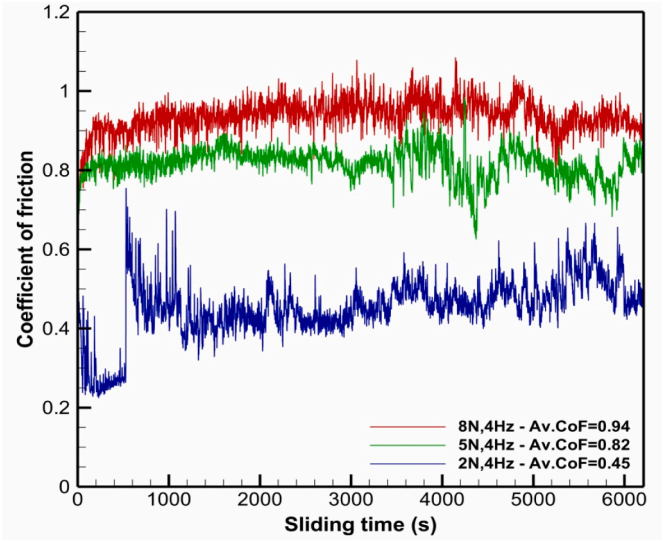

Fig. 9. Evolution of the coefficient of friction with sliding time for NiTiNOL60 alloy sliding against Al_2O_3 ball at different applied loads.

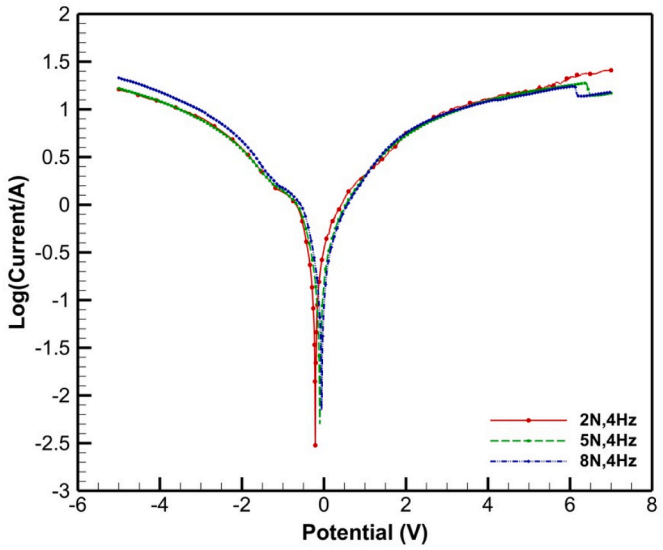

Fig. 10. Potentiodynamic polarisation curves of NiTiNOL60 at different load conditions.

3.2. Frictional behaviour and the effect of sliding contact on electrochemical potential

The variations of the coefficient of friction (CoF) with time for samples tested under different loads were recorded from the tribometer via WINDUCOM software, and the results are presented in Fig. 9. From the plot, it could be seen that the CoF increases as the applied load increase; thereby resulting in more wear and different wear mechanisms along the wear track. The graphical trend for 2 N load shows a running-in time within the sliding time of 500 s which shows there was no adequate contact pressure from the applied load. After the barrier, the counter material was able to wear off the passive oxide layer and penetrate the NiTiNOL60 sample thus maintaining a relatively stable CoF. Whereas at higher loads, almost no running-in was recorded until the curves attained a steady state. According to Ref. [30]; the recorded trend can be attributed to partial rebuilding of passivation film under sliding contact, but the partial rebuilding becomes difficult at larger normal loads. Irrespective of the higher wear rate, the samples displayed more stable friction coefficients at higher loads. The relatively stable CoF trend could be a result of dynamic equilibrium between electrochemical passivation and mechanical passivation during tribocorrosion. This also indicates that the passive film is gradually destroyed during the sliding contact as reported previously by Ref. [30]. The results presented in Figs. 6 and 7 showed the adherence of the NiTiNOL60 material onto the ball surface, which impacts the surface roughness in the contact interface. The introduction of this roughness, due to the micro-scale material transfer during the wear process, resulted in fluctuating frictional behaviour presented in Fig. 9.

Table 3
Tafel fitting parameters of NiTiNOL60 at different normal loads.

Sample	E_{corr} (V)	I_{corr} (A) × 10^{-3}	R_p (Ω)	Corrosion Rate (mmpy)
NiTiNOL60 – 2N, 4Hz	−1.7364	1.104	812.5	0.868
NiTiNOL60 – 5N, 4Hz	−1.4401	2.277	487.1	1.790
NiTiNOL60 – 8N, 4Hz	−0.2730	2.810	294.9	2.209

The Tafel curves obtained after the OCP and during potentiodynamic polarisation measurements are represented in Fig. 10. In an electrochemical system, the corrosion potential indicates the corrosion tendency of an alloy and is determined by its constituent elements with different electrode potentials [6]. This implies that the higher the electrode corrosion potential, the weaker the corrosion tendency. As shown in Fig. 10, the curves depict a clear passivation platform area, indicating that a stable passivation film is formed on the surface of the material within the corresponding self-corrosion potential range in order to protect the surface from localised corrosion [41,42]. According to Ref. [43]; the OCP or corrosion potential (E_{corr}), which promotes passivation, is the potential created by the electrochemical processes at a metal surface immersed in a solution.

From the plots, it is evident that E_{corr} for 2 N load is more negative when compared to the 8 N load while the I_{corr} increased with load increase. As a result, a higher corrosion rate was recorded at higher load, and this clearly indicates the promoting effect of sliding contact on corrosion.

The corrosion potential, corrosion current density and the corrosion rate, summarised in Table 3, were obtained through the standard Tafel measurements using Ivium software. The open circuit potential represents the electrochemical activity of the material at the various conditions investigated. It shows that the potential of the sample is more negative at lower loads which indicates that higher loads accelerate the electrochemical activity. This shows that open circuit stabilisation occurred at the cathodic region, whereas the wear recorded in the anodic regime contributed to the significant corrosion current density.

From the results in Table 3, the corrosion potential at different loads investigated is lower, which means they corrode faster though the corrosion rate and corrosion currents are lower. This implies the repassivation layer significantly enhanced the corrosion resistance under the exposed conditions of the metal-solution interface thereby causing the surface of the metal to corrode.

The surface conditions of NiTi-based alloys are known to strongly influence the corrosion behaviour, particularly passivity [31,44,45]. Moreover, the corrosion resistance of NiTi-based alloy is related to the formation of the titanium oxide film. The parameters outlined in Table 3, reveal that the corrosion resistance decreased with load increase, yet possess a stronger ability to form an oxide film. Du et al. [6] reported that the corrosion tendency is weaker at higher corrosion potentials. However, Table 3 shows that a higher corrosion rate is established in this investigation following a higher shear deformation which allows more wear and creates larger surface area for corrosion to occur thus reducing the protective effect of the passive film. Overall, it is evident that corrosion rate increased with load increase. While corrosion

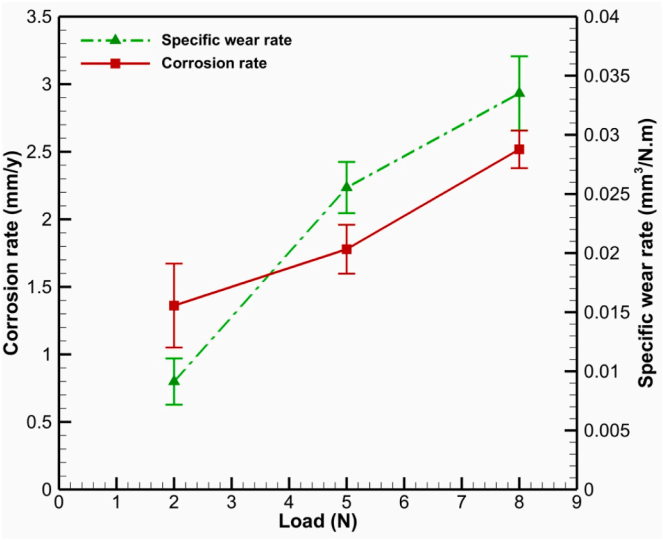

Fig. 11. Specific wear rates and corrosion rates at different normal loads.

potential and corrosion current density are seen to increase with load increase, the resistance is the reverse thus, leading to increased corrosion rate. According to Ref. [6]; the electrode potential difference could equally be affected by the different phases in NiTi-based alloys. As a result, the dominance of Ni_4Ti_3 phase bequeaths corrosion resistance to the NiTiNOL60 alloy.

3.3. Wear mechanisms

Following the analysis above, it is evident that wear due to sliding contact would result in accelerated corrosion. It is therefore imperative that the possible mechanisms occurring during the tribocorrosion be determined. From the SEM images of the samples under tribocorrosion test at different load conditions, various wear mechanisms were recorded. Fig. 11 shows a summarised plot for the mechanical wear and chemical corrosion, respectively. The specific wear rate as well as the corrosion rate increased with load increase, and this follows the existing literature information [6,30].

Fig. 11 shows that corrosion rate increases with load. This is attributed to the amount of contact pressure made on the surface during the reciprocal sliding wear. Hence, at higher loads, continuous sliding results in enhanced shear deformation, thereby destroying the passive films/layers and exposing fresh layers which are easily attacked in the electrolyte. In line with the findings of [30] it is clearly indicated that

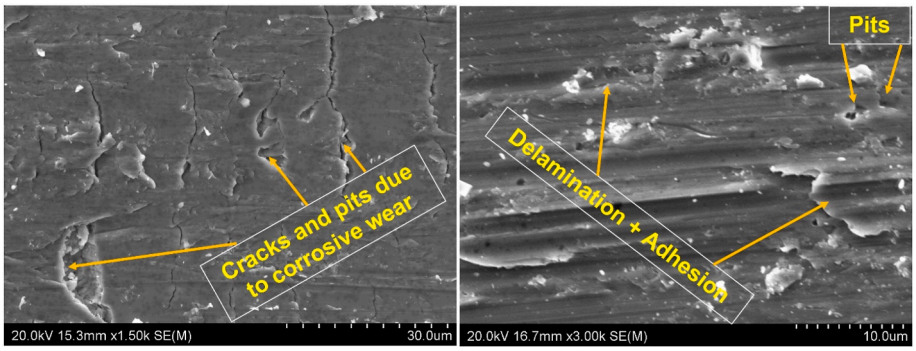

Fig. 12. SEM images showing third-body effect and microcracks at 8 N load on NiTiNOL60 alloy.

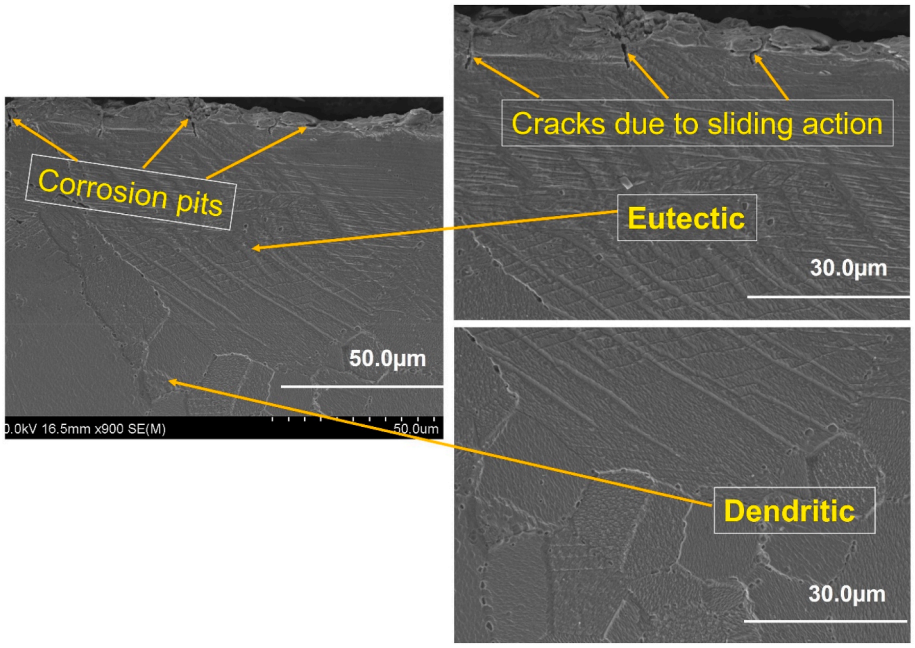

Fig. 13. SEM microstructure of the cross-sectional view of etched NiTiNOL60 sample.

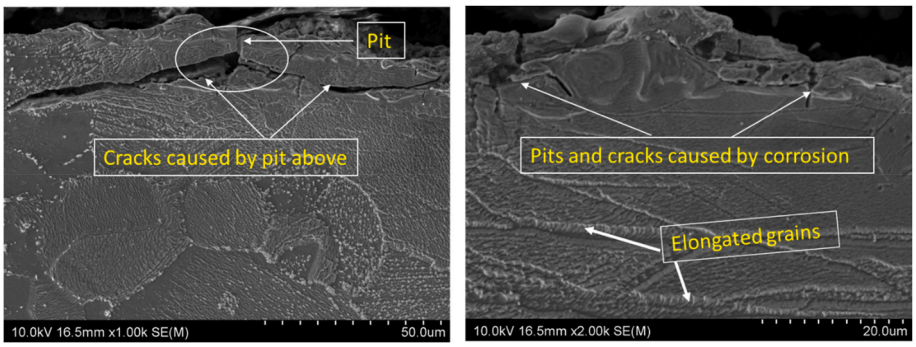

Fig. 14. SEM microstructure of the cross-sectional view of NiTiNOL60 wear track.

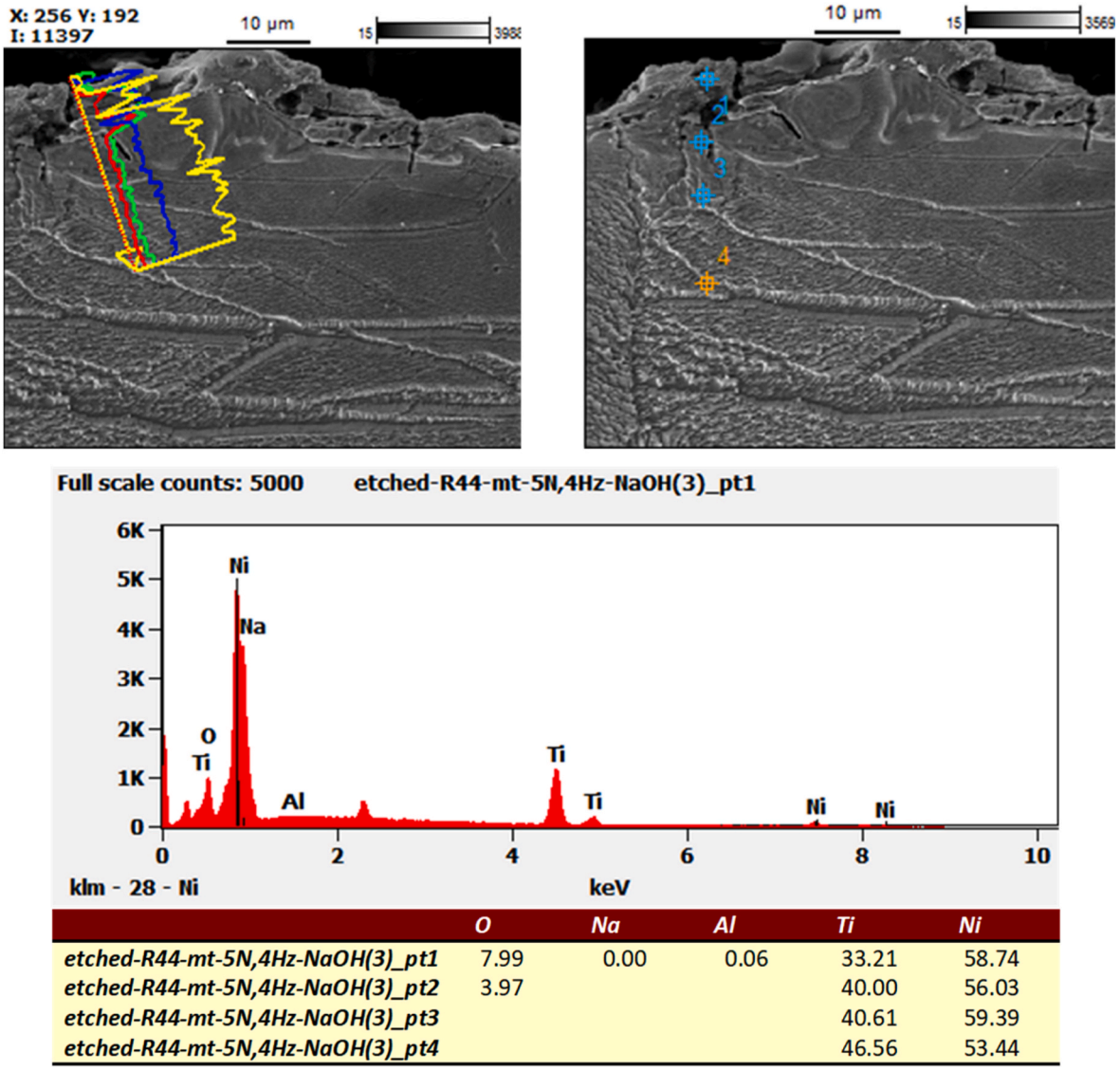

	O	Na	Al	Ti	Ni
etched-R44-mt-5N,4Hz-NaOH(3)_pt1	7.99	0.00	0.06	33.21	58.74
etched-R44-mt-5N,4Hz-NaOH(3)_pt2	3.97			40.00	56.03
etched-R44-mt-5N,4Hz-NaOH(3)_pt3				40.61	59.39
etched-R44-mt-5N,4Hz-NaOH(3)_pt4				46.56	53.44

Fig. 15. SEM and EDS analyses of the etched sample using line and point scans x-ray.

delamination wear was caused by the exfoliation of oxide during sliding contact, which ultimately leads to the aggravation of corrosion.

The high volume of material loss due to sliding contact is supported by t he SEM images in Fig. 12 where a significant contribution from a third-body wear is recorded following the patterns of the abrasion grooves, micro striation, delamination and debris adhesion. These impacts result in less significant material loss due to the electrochemical corrosion. Therefore, the presence of TiO_2 film formation coupled with the excellent self-healing ability of Ni–Ti alloys [6,46] helped to promote a better corrosion resistance of the sample. Further, Du et al. [6] highlighted that appropriate passivation results in the build-up of TiO_2 (a very stable protective layer), which hinders ion exchange.

To ascertain the level of deformation and the likely impact on the sample's microstructure, the cross-section of the tested samples was cut under the wear track, etched, and observed under SEM. Fig. 13 shows the surface examination and the microstructure of the cross-sectional parts of the wear track. From the images, the sample is noted to have more of eutectic network structure within 100 μm into the sample cross-section as a result of sliding shear deformation, while the dendritic clusters dominate the lower surfaces of the cross-section. Following the distortion of the grain boundaries, it is evident that the microcracks and pits exists around the edges of the cross-sectional surface due to the corrosion attack [47]. As shown in the image, the microcracks initiated from the corrosion pits which penetrated beyond the surface of the sample, but its propagation falls within 120 μm of the sample surface. Corrosion pits and cracks occurred as a result of the electrochemical reactions, while the tribological impact as a result of the reciprocating sliding and the increased temperature due to continuous sliding clearly shows the grain elongation in the direction of sliding action as shown in Fig. 14. Thus, the sliding contact has been deduced to accelerate corrosion.

As the passive films are easily destroyed because of sliding action, the interfaces of phase NiTi matrix show more susceptibility to pitting. However, the formation of dense oxide film at lower loads could be attributed to the uniform microstructure and fine dendritic microstructure of the sample since the applied load has less contact pressure to wear off significant amount of the sample during sliding. Consequently, a report by Vandenkerhove in Ref. [6] highlighted that a nickel-titanium alloys containing mainly NiTi phase showed a lower corrosion intensity.

Fig. 15 shows the EDS result obtained from a line-scan and point-scan x-rays carried out to determine the level of damage or penetration caused by the oxide layer. While the line-scan identified elements such as oxygen, sodium, titanium and nickel, the point and shoot scan presents elements like oxygen, aluminium, titanium and nickel. The different coloured lines denote the concentration of the elements thus, the yellow and blue lines highlight the higher concentration of the parent elements Ni and Ti. The green, red, and orange lines show traces of O_2, Na and Al within the region scanned i.e., the oxidised location. The point-scan further confirmed the identified elements by line-scan and their corresponding wt.% in as shown in the accompanying table in Fig. 15.

From the table, the percentage of Al debris only appeared on the top surface and within the oxide layer region. The oxide film exits only at points 1 and 2 as shown by the point and shoot scan, whereas the parent material Ni and Ti are recorded at the 4 different points investigated. This supports the explanation under Fig. 13 that the propagation of cracks and crevices do not penetrate beyond 120 μm of the material surface (particularly the oxide layer region). The change in Ni–Ti wt.% composition recorded at point 4 could be attributed to the grain elongation around the spot.

4. Conclusions

This study investigated the behaviour and the effects of sliding wear and electrochemical potential of NiTiNOL60 alloy in alkaline environment (0.05 M NaOH (aq)) under varied normal loads sliding against Al_2O_3 counter-body on a ball-on-plate tribometer configuration. In the sample characterisation, SEM imaging and EDS analysis authenticated the composition of the NiTiNOL60 sample, confirming it as a non-equiatomic material with a weight percentage composition of 60% Ni and 40% Ti. The material exhibited a cubic crystal structure matrix, with consolidated and unconsolidated regions in its microstructural grains, suggesting the possibility of Ni-rich or Ti-rich zones. From the study it is evident that increase in load results in accelerated corrosion. The results reveal a distortion of the microstructure grains due to sliding action and the wear mechanisms on the tribological wear track. Further, increase in applied load leads to the deterioration of oxide film formed along the wear track due to the higher relative motion between the contact surfaces and this significantly increases the wear rate of the material under higher loading conditions. This results in a cathodic shift in the potentiodynamic measurements and a higher resistance, thereby leading to a lower corrosion rate. The results from surface examinations presented various wear mechanisms, including abrasion, adhesion, fatigue and oxidative wears as seen along the wear track. However, the mechanisms of abrasive wear which involves cutting, fracture, fatigue and grain pull-out were predominant especially at higher normal loads.

Declaration of competing interest

The authors declare that they have no known competing financial interests or personal relationships that could have appeared to influence the work reported in this paper.

Data availability

Data will be made available on request.

References

[1] M.J. Carrington, J.L. Daure, V.L. Ratia-Hanby, D. Zhang, P.H. Shipway, D. A. Stewart, D.G. McCartney, Microstructural characterisation of subsurface deformation and the degradation of Stellite 6 induced by self-mated sliding contact in a simulated PWR environment [Article], Tribol. Int. 158 (2021), 106899, https://doi.org/10.1016/j.triboint.2021.106899.
[2] F. Ropital, Corrosion and Degradation of Metallic Materials : Understanding of the Phenomena and Applications in Petroleum and Process Industries, Editions Technip, 2010.
[3] H. Duan, Y. Wu, M. Hua, C. Yuan, D. Wang, J. Tu, H. Kou, J. Li, Tribological properties of AlCoCrFeNiCu high-entropy alloy in hydrogen peroxide solution and in oil lubricant, Wear 297 (1–2) (2013) 1045–1051, https://doi.org/10.1016/j.wear.2012.11.014.
[4] S. Varmaziar, M. Atapour, Y.S. Hedberg, Corrosion and metal release characterization of stainless steel 316L weld zones in whey protein solution, npj Materials Degradation 6 (2022) 1–9, https://doi.org/10.1038/s41529-022-00231-7.
[5] P.J. Blau, R. Wood, M.M. Stack, S. Mischler, J. Jiang, D. Drees, L.A. Rocha, M. A. Wimmer, J.P. Celis, R. Cowan, Future Needs and Challenges in Tribo-Corrosion Research and Testing, ASTM Special Technical Publication, 2013.
[6] Z. Du, Z. Hu, Y. Feng, F. Mo, The effect of powder composition on the microstructure and corrosion resistance of laser cladding 60NiTi alloy coatings on SS 316L, Metals 11 (7) (2021), https://doi.org/10.3390/met11071104.
[7] R.C.C. Silva, R.P. Nogueira, I.N. Bastos, Tribocorrosion of UNS S32750 in chloride medium: effect of the load level, Electrochim. Acta 56 (24) (2011) 8839–8845, https://doi.org/10.1016/j.electacta.2011.07.077.
[8] M. Atapour, I. Odnevall Wallinder, Y.S. Hedberg, Stainless steel in simulated milk and whey protein solutions - influence of grade on corrosion and metal release, Electrochim. Acta 331 (2020), 135428, https://doi.org/10.1016/j.electacta.2019.135428.
[9] A. Zaffora, F.D. Franco, M. Santamaría, Corrosion of stainless steel in food and pharmaceutical industry, Current Opinion in Electrochemistry (2021), 100760, https://doi.org/10.1016/J.COELEC.2021.100760.
[10] S. Cao, S. Mischler, Tribocorrosion of a CoCrMo alloy in sulfuric acid – glycerol mixtures, Wear (2020) 458–459, https://doi.org/10.1016/j.wear.2020.203443.
[11] A. Siddaiah, A. Kasar, R. Ramachandran, P.L. Menezes, Introduction to tribocorrosion, in: A. Siddaiah, R. Ramachandran, P.L. Menezes (Eds.), Tribocorrosion: Fundamentals, Methods, and Materials, Academic Press, 2021, pp. 1–16, https://doi.org/10.1016/B978-0-12-818916-0.00002-X.
[12] J. Chen, H. Mraied, W. Cai, Determining tribocorrosion rate and wear-corrosion synergy of bulk and thin film aluminum alloys, JoVE 2018 (139) (2018), https://doi.org/10.3791/58235.
[13] C. Miller, C. DellaCorte, M. Zou, Nanomechanical properties of hardened 60NiTi, Mater. Sci. Eng. 800 (2021), https://doi.org/10.1016/j.msea.2020.140284.
[14] W.J. Buehler, F.E. Wang, A summary of recent research on the nitinol alloys and their potential application in ocean engineering, Ocean Eng. 1 (1) (1968) 105–120.
[15] C. DellaCorte, *NiTi Alloys for Tribological Applications: The Effects of Serendipity on Research and Development* Annual Postdoctoral Research and Career Symposium (No, GRC-E-DAA-TN34568, 2016.
[16] L.A. Dobrzański, L.B. Dobrzański, A.D. Dobrzańska-Danikiewicz, J. Dobrzańska, Nitinol type alloys general characteristics and applications in endodontics, Processes 10 (1) (2022), 101, https://doi.org/10.3390/pr10010101.
[17] O. Benafan, A. Garg, R.D. Noebe, H.D. Skorpenske, K. An, N. Schell, Deformation characteristics of the intermetallic alloy 60NiTi, Intermetallics 82 (2017) 40–52, https://doi.org/10.1016/j.intermet.2016.11.003.
[18] M.K. Stanford, Hardness and Microstructure of Binary and Ternary Nitinol Compounds, No. GRC-E-DAA-TN73728, 2019.
[19] J.L. Jeronimo, A.P. Krelling, C. Pacheco, I. Bonetti, R. da Silva, J.C.G. Milan, C. E. da Costa, Microstrutural, mechanical characterizations and corrosion behaviour

of borides layers on Inconel 718 superalloy, Results in Engineering 16 (2022), 100783, https://doi.org/10.1016/j.rineng.2022.100783.
[20] L.A. Khan, E. McCarthy, C. Muilwijk, I.U. Ahad, D. Brabazon, Analysis of nitinol actuator response under controlled conductive heating regimes, Results in Engineering 18 (2023), 101047, https://doi.org/10.1016/j.rineng.2023.101047.
[21] M.V. Rahul, V. Balaji, S. Narendranath, Optimization of wire-EDM process parameters for Ni–Ti-Hf shape memory alloy through particle swarm optimization and CNN-based SEM-image classification, Results in Engineering 18 (2023), 101141, https://doi.org/10.1016/j.rineng.2023.101141.
[22] C. DellaCorte, R.D. Noebe, M.K. Stanford, S.A. Padula, Resilient and Corrosion-Proof Rolling Element Bearings Made from Superelastic Ni-Ti Alloys for Aerospace Mechanism Applications, 1542 STP, ASTM Special Technical Publication, 2011, pp. 143–166, https://doi.org/10.1520/STP103887. No. NASA/TM-2011-217105.
[23] M. Elahinia, N. Shayesteh Moghaddam, M. Taheri Andani, A. Amerinatanzi, B. A. Bimber, R.F. Hamilton, Fabrication of NiTi through additive manufacturing: a review, Prog. Mater. Sci. 83 (2016) 630–663, https://doi.org/10.1016/j.pmatsci.2016.08.001.
[24] E.O. Ezugwu, Z.M. Wang, A.R. Machado, The machinability of nickel-based alloys: a review, J. Mater. Process. Technol. 86 (1–3) (1998) 1–16, https://doi.org/10.1016/S0924-0136(98)00314-8.
[25] S. Ingole, 60NiTi alloy for tribological and biomedical surface engineering applications, JOM Journal of the Minerals Metals and Materials Society 65 (6) (2013) 792–798, https://doi.org/10.1007/s11837-013-0610-7.
[26] D. Kapoor, Nitinol for medical applications: a brief introduction to the properties and processing of nickel titanium shape memory alloys and their use in stents, Johnson Matthey Technology Review 61 (1) (2017) 66–76, https://doi.org/10.1595/205651317x694524.
[27] C. DellaCorte, Nickel-Titanium alloys: corrosion “proof” alloys for space bearing, components and mechanism applications, in: 40th Aerospace Mechanisms Symposium, 2010, E-17269.
[28] L. Zhang, H. Peng, Q. Qin, Q. Fan, S. Bao, Y. Wen, Effects of annealing on hardness and corrosion resistance of 60NiTi film deposited by magnetron sputtering, J. Alloys Compd. 746 (2018) 45–53, https://doi.org/10.1016/j.jallcom.2018.02.227.
[29] T. Kosec, P. Močnik, A. Legat, The tribocorrosion behaviour of NiTi alloy, Appl. Surf. Sci. 288 (2014) 727–735, https://doi.org/10.1016/j.apsusc.2013.10.116.
[30] C. Yan, Q. Zeng, Y. Xu, W. He, Microstructure, phase and tribocorrosion behavior of 60NiTi alloy, Appl. Surf. Sci. 498 (2019), https://doi.org/10.1016/j.apsusc.2019.143838.
[31] H. Chen, Z. Zhang, X.H. Hao, B.X. Huang, X.C. Zhao, C.C. Hu, Microstructure and tribocorrosion properties of NiTi/AlNi2Ti ternary intermetallic alloy, Vacuum 184 (2021), https://doi.org/10.1016/j.vacuum.2020.109928.
[32] W. Xu, A. Yu, X. Lu, M. Tamaddon, L. Ng, M. Dilawer Hayat, M. Wang, J. Zhang, X. Qu, C. Liu, Synergistic interactions between wear and corrosion of Ti-16Mo orthopedic alloy, J. Mater. Res. Technol. 9 (5) (2020) 9996–10003, https://doi.org/10.1016/j.jmrt.2020.06.095.
[33] S.B. Arya, F.J. Joseph, Electrochemical methods in tribocorrosion, in: A. Siddaiah, R. Ramachandran, P.L. Menezes (Eds.), Tribocorrosion, Academic Press, 2021, pp. 43–77, https://doi.org/10.1016/B978-0-12-818916-0.00003-1.
[34] ASTM G3 - 14, Standard Practice for Conventions Applicable to Electrochemical Measurements in Corrosion Testing, American Society for Testing and Materials, Annual Book of ASTM Standards, 2019, https://doi.org/10.1520/g0003-14.
[35] ASTM G119 - 09, Standard Guide for Determining Synergism between Wear and Corrosion, American Society for Testing and Materials, Annual Book of ASTM Standards, 2016, https://doi.org/10.1520/g0119-09r16.
[36] ASTM G133 - 02, Standard test method for linearly reciprocating ball-on-flat sliding wear, in: American Society for Testing and Materials, vol. 5, Annual Book of ASTM Standards, 2017.
[37] M.T. Mathew, M.A. Wimmer, Tribocorrosion in artificial joints: in vitro testing and clinical implications, in: Bio-Tribocorrosion in Biomaterials and Medical Implants, 2013, pp. 341–371, https://doi.org/10.1533/9780857098603.3.341.
[38] K. Khanlari, M. Ramezani, P. Kelly, P. Cao, T. Neitzert, Mechanical and microstructural characteristics of as-sintered and solutionized porous 60NiTi, Intermetallics 100 (2018) 32–43, https://doi.org/10.1016/j.intermet.2018.06.001.
[39] F.O. Pessu, E. Saleem, C. Espejo, A. Neville, Understanding the local pitting corrosion characteristics of carbon steel in CO2 corrosion environment using artificially machined pits, Results in Engineering 16 (2022), 100700, https://doi.org/10.1016/j.rineng.2022.100700.
[40] J.Z. He, J.N. Lu, X.Y. Deng, X.Q. Xing, Z.C. Luo, Premature fracture of high-strength suspension springs caused by corrosion fatigue cracking, Results in Engineering 16 (2022), 100749, https://doi.org/10.1016/j.rineng.2022.100749.
[41] J.P. Celis, P. Ponthiaux, Testing tribocorrosion of passivating materials supporting research and industrial innovation: a handbook. https://www.scopus.com/inward/record.uri?eid=2-s2.0-85122845713&partnerID=40&md5=9dec03e568e7b11f8acb602d535d13a2, 2017.
[42] J.P. Celis, P. Ponthiaux, F. Wenger, Tribo-corrosion of materials: interplay between chemical, electrochemical, and mechanical reactivity of surfaces, Wear 261 (9) (2006) 939–946, https://doi.org/10.1016/j.wear.2006.03.027.
[43] S. Alkan, M.S. Gök, Effect of sliding wear and electrochemical potential on tribocorrosion behaviour of AISI 316 stainless steel in seawater, Engineering Science and Technology, an International Journal 24 (2) (2021) 524–532, https://doi.org/10.1016/j.jestch.2020.07.004.
[44] I. García, D. Drees, J.P. Celis, Corrosion-wear of passivating materials in sliding contacts based on a concept of active wear track area [Article], Wear 249 (5–6) (2001) 452–460, https://doi.org/10.1016/S0043-1648(01)00577-4.
[45] R. Neupane, Z. Farhat, Wear mechanisms of NiTinol under reciprocating sliding contact, Wear 315 (1–2) (2014) 25–30, https://doi.org/10.1016/j.wear.2014.02.018.
[46] A.I. Muñoz, N. Espallargas, Tribocorrosion Mechanisms in Sliding Contacts, 2011.
[47] A. López-Ortega, R. Bayón, J.L. Arana, Evaluation of protective coatings for offshore applications. Corrosion and tribocorrosion behavior in synthetic seawater, Surf. Coating. Technol. 349 (2018) 1083–1097, https://doi.org/10.1016/j.surfcoat.2018.06.089.
[48] S.V. Pepper, C. DellaCorte, R.D. Noebe, D.R. Hull, G. Glennon. Nitinol 60 as a material for spacecraft triboelements, European Space Agency, (Special Publication) ESA SP, 2009.
[49] K. Khanlari, M. Ramezani, P. Kelly, P. Cao, T. Neitzert, Reciprocating Sliding Wear Behavior of 60NiTi As Compared to 440C Steel under Lubricated and Unlubricated Conditions, Tribology Transactions 61 (6) (2018) 991–1002. https://doi.org/10.1080/10402004.2018.1460434.
[50] K. Khanlari, M. Ramezani, P. Kelly, P. Cao, T. Neitzert, Comparison of the reciprocating sliding wear of 58Ni39Ti-3Hf alloy and baseline 60NiTi, Wear 408–409 (2018) 120–130. https://doi.org/10.1016/j.wear.2018.05.011.
[51] K. Khanlari, M. Ramezani, P. Kelly, P. Cao, T. Neitzert, Mechanical and microstructural characteristics of as-sintered and solutionized porous 60NiTi, Intermetallics 100 (2018) 32–43. https://doi.org/10.1016/j.intermet.2018.06.001.
[52] K. Khanlari, M. Ramezani, P. Kelly, M. Hayat, P. Cao, T. Neitzert, An investigation on microstructural and mechanical properties of porous 60NiTi parts solutionized by different cost-effective methods, Metallography, Microstructure & Analysis 7 (3) (2018) 334–346. https://doi.org/10.1007/s13632-018-0443-4.